PAPER

A facile and surfactant-free route for nanomanufacturing of tailored ternary nanoalloys as superior oxygen reduction reaction electrocatalysts†

Sheng Hu,[bcd] Kangming Cheng,[ac] Erick L. Ribeiro,[bcd] Kiman Park,[bc] Bamin Khomami *[abd] and Dibyendu Mukherjee (iD) *[abcd]

We have synthesized ternary nanoalloys (NAs) of Pt with transition metals (Co, Cu, Ni, Ti, Ru, Mn) as oxygen reduction reaction (ORR) electrocatalysts using our recently developed laser ablation synthesis in solution-galvanic replacement reaction (LASiS-GRR) technique as a facile and surfactant-free nanomanufacturing route. The specific choice of the elemental compositions is driven by the respective target metal/metal salt redox potential gaps as well as the target metal and/or metal oxide solubility in desired acids. The high-energy thermodynamics of the LASiS-GRR process enables control of the sizes, elemental compositions and distributions of the ternary NAs through systematic tuning of the initial metal salt concentration, pH, laser fluence and ablation time. Specifically, the PtCuCo NAs synthesized with an elemental composition of 72 : 12 : 16 (Pt : Co : Cu) exhibit the best ORR catalytic activity. The NAs largely possess a shell–core structure with the shell composed mostly of Pt and a minor amount of Cu, along with a uniformly alloyed PtCuCo core. Mass and specific activities for ORR performance of the NAs indicate a 4- and 6.5-fold improvement, respectively, over the corresponding activities of commercial Pt/C. We attribute the enhanced activity to 1) our surfactant/ligand-free synthesis technique that prevents catalytic site degradation and 2) minor alloying of the second transition metal Cu that shifts back the Pt d-band center to an optimal position between those of Pt and the PtCo binary NAs, thereby tuning their binding affinities for both oxygen and oxygenated species. Finally, this work establishes the versatility of the LASiS-GRR technique through the synthesis of other ternary NAs (PtRuNi, PtCoMn, PtNiTi) that also exhibit reasonably good ORR activities.

[a] Department of Mechanical, Aerospace & Biomedical Engineering, University of Tennessee, Knoxville, Tennessee, 37996, USA. E-mail: bkhomami@utk.edu, dmukherj@utk.edu; Tel: +86 5974 2035, +86 5974 5309
[b] Department of Chemical & Biomolecular Engineering, University of Tennessee, Knoxville, Tennessee, 37996, USA
[c] Nano-BioMaterials Laboratory for Energy, Energetics & Environment (nbml-E³), University of Tennessee, Knoxville, Tennessee, 37996, USA
[d] Sustainable Energy Education & Research Center (SEERC), University of Tennessee, Knoxville, Tennessee, 37996, USA
† Electronic supplementary information (ESI) available. See DOI: 10.1039/c7cy00073a

1. Introduction

Proton exchange membrane fuel cells (PEMFCs) have gained tremendous research interest in recent years[1–3] owing to the quest for sustainable carbon-neutral energy sources to address the surge in global energy consumption. However, the critical bottleneck in the commercialization of PEMFCs lies in the facile and cost-effective synthesis of electrocatalysts to facilitate the rate-determining oxygen reduction reactions (ORRs) at the cathode.[4,5] To this end, PtM (where M stands for transition metals such as Co, Cu, Ni, Ru, Pd, Au, *etc.*) nanoalloys (NAs) have found a prominent place in the PEMFC community as well-known ORR electrocatalysts that exhibit comparable and, in some cases, even better catalytic performances while lowering the precious metal contents.[1,2,6–12] This enhanced catalytic activity is attributed to the synergistic geometric and electronic effects arising inherently from the alloying process. The former effect refers to the shrinkage of lattice parameters that increases the number of active surface sites for catalysis, while the latter is attributed to the shift in the atomic d-band centers that results in proper tuning of the binding affinities for both oxygen and intermediate oxygenated species such as O*, OH*, OOH*, *etc.*[13–17] Moreover, alloying is aimed at promoting the oxygen adsorption process by enhancing the Pt–O affinity while simultaneously facilitating the dissociation of intermediate oxygenated species from the Pt surface.[5,18–20] It has been reported that alloying Pt with transition metals on the left-hand side of the Pt column (group 10) will generally downshift the d-band center and

weaken the Pt–O binding affinity. On the other hand, alloying Pt with transition elements to the right of group 10 mostly shifts up the Pt d-band center and lowers the energy barrier for binding oxygen.[14,15,21] However, in either case, the common challenge is the optimization of the binding affinities for both oxygen/intermediate oxygenated species by simply alloying Pt with a single transition metal.[9,10,22]

In light of the aforementioned challenges, recent efforts have been directed towards the use of multiple transition metals for fine-tuning the two competing binding processes and hence the molecular affinities.[14–17,21,23–25] To this end, the proposed effective alloying has involved the combinations of noble metals with a series of 3-d to 5-d transition metals such as PtAu(Co, Pd),[14,20,26] PtNi(Cu, Co, Fe, Cr),[5,18,27,28] PtPd(Co, Ni, Cu),[24,28,29] PtFe(Cu, V, Ni, Co),[30–34] PtCo(Cr, Ir, Ni),[35–38] PtMn(Fe, Co, Ni, Cu, Mo, Sn),[39] PtCu(Te, Co),[16,40] etc. However, the synthesis routes for most of these intermetallic compounds are chemically based which inevitably involve unwanted surfactants and stabilizing/reducing agents during the complex processing steps that can potentially block the active interfacial sites and hence impede catalytic activities.[41,42] Furthermore, post-processing steps for the removal of these unwanted chemicals require even harsher conditions such as high-temperature treatment that might induce severe agglomeration of the NAs.

To this end, previously we have reported the successful use of pulsed laser ablation synthesis in solution (LASiS)/laser ablation in liquid (LAL) for the synthesis of metal/metal oxide nanostructures[43] and, more specifically, our newly developed LASiS in tandem with galvanic replacement reaction (LASiS-GRR) technique as a clean (surfactant/ligand-free), facile method with low startup cost for the synthesis of Pt–Co-based nanocomposites (NCs) and pure NAs.[44,45] Specifically, the pure NAs were synthesized by modifying this technique to include real-time moderate acid treatments right after LASiS-GRR to wash away the superfluous cobalt oxides with minimal leaching of the alloyed Co.[44] During LASiS-GRR, a pulsed laser beam aimed at a metal target vaporizes the target surface through photoionization and creates a liquid-confined plasma plume with extreme temperatures ($\sim$5000 K) and pressures ($\sim$10 MPa). This in turn creates a cavitation bubble containing seeding target NPs that nucleate, expand and propagate at an ultrafast speed ($>10^3$ m s^{-1}).[46–50] It needs to be mentioned here that the exact reaction pathways emerging out of laser–matter interactions inside the plasma plume and cavitation bubble are still an area of active research. However, a few recent in situ spatio-temporal analyses of laser-induced plasma emissions and/or scattering techniques during laser ablation synthesis have indicated that solutes/ions can also be present in the cavitation bubble, thereby initiating the GRR processes during the target plasma quenching and nucleation.[51–55] Besides, Ayumu Matsumoto et al. also proposed that it is the phase explosion of water due to the strong interaction with the high-temperature plasma that leads to the incorporation of ions in the initial bubbles.[51] On the other hand, in a recent review article,

Dongshi Zhang et al. suggested the presence of ionic species in the supercritical vapor surrounding the plasma plume in the early stages of cavitation bubbles, which can take part in GRR and other chemical reactions.[56] Thereafter, the reduced precursor metal atoms/nuclei quickly alloy with the remaining and newly quenched target metal atoms to form intermetallic NAs.[44,45] Once the internal pressure decreases to that of the surrounding liquid, the bubble collapses at a time scale of hundreds of microseconds,[57–61] thereby enabling the seeding intermetallic NAs to further grow and agglomerate at the bubble–liquid interface.[62–64] The unique advantages of the LASiS-GRR technique stem from the extreme out-of-equilibrium conditions inside the laser-induced plasma plume and cavitation bubbles wherein GRR occurs simultaneously with NA nucleation, with conceivable laser irradiation to assist the whole process.[46,50,65–71] This consequently provides the produced NPs with uniform elemental distributions as well as plasma-induced surface charges that potentially prevent their severe agglomeration without the need for any surfactant.[44,70] Additionally, the rational tuning of the produced NA compositions in terms of elemental ratio and degree of alloying becomes achievable by adjusting the laser (laser fluence, wavelength, ablation time) as well as environmental parameters (salt concentrations, temperature, pH).[44]

The work presented in this article aims at developing LASiS-GRR into a more versatile technique for the synthesis of complex higher-order ternary nano-alloyed structures with varied compositions and alloying as ORR electrocatalysts. In light of their application as low precious metal loading PEMFC catalysts, the surfactant-free LASiS-GRR technique involving extreme plasma-confined physicochemical conditions provides tremendous potential for carrying out the fine-tuning of the respective elemental ratios via simple experimental parameters. Specifically, we report the synthesis of Pt-based ternary NAs. In turn, the facile yet surfactant-free synthesis technique presented here is used to achieve the aforementioned optimization of the binding affinities between Pt and oxygen/oxygenated species in order to achieve the best ORR catalytic activity.

2. Experimental details

Materials and methods: Co, Ni, Mn and Ti pellets were bought from Kurt J. Lesker (99.95% purity, 1/4″ diameter × 1/4″ height) and all the metal precursor salts (i.e., K_2PtCl_4, CuCl, $CoCl_2$, $NiCl_2$), HCl and KOH were bought from Sigma-Aldrich. LASiS-GRR experiments were carried out in an in-house built laser ablation cell equipped with facilities for simultaneous injection of metal salt solutions, temperature control as well as ultrasonication, as depicted in detail in our earlier work.[72] For the synthesis of Pt-based ternary NAs, a freshly prepared K_2PtCl_4 solution along with the second precursor salt solution was transferred into the LASiS cell through the injection unit. The target metal, while being rotated by a stepper motor at a uniform speed of 0.3 rpm, was ablated using an unfocused 1064 nm pulsed Nd-YAG laser

This journal is © The Royal Society of Chemistry 2017

Catal. Sci. Technol., 2017, 7, 2074–2086 | 2075

(330 mJ per pulse, 10 Hz) for various times. Right after ablation, the pH of the produced colloidal solution was adjusted by adding HCl followed by aging in darkness for 24 hours. Finally, the ternary NAs were collected by centrifugation at 4700 rpm for 15 min and decanted after washing with DI-water two times. For LASiS-GRR at pH 11 (PtCuCo-4), KOH was used for preparing the alkaline solution, with the synthesis and post-treatment procedures being the same as those under the neutral conditions. Besides, all the LASiS-GRR experiments mentioned above were carried out at room temperature with simultaneous probe ultrasonication.

2.1 Synthesis of ternary NAs

The detailed synthesis parameters are summarized in Tables 1 (for PtCo and various PtCuCo NAs) and S3† (for different categories of Pt-based ternary alloys). Two specified LASiS-GRR methods are proposed and compared for synthesizing PtCuCo ternary NAs in the current work, namely, 1) using two metal precursor salts (K_2PtCl_4 and CuCl in this case) for ablation on Co simultaneously (*a one-step technique*) and 2) using two metal targets (Co and Cu) for ablation in K_2PtCl_4 solution alternately (*two or multi-step technique*). The latter route was found to produce NAs with less uniform elemental distribution and ORR catalytic activity and has been discussed in detail in the ESI.† The former one-step technique is made possible by the rational choice of metal targets/metal salts with optimal redox potential differences. Specifically, the redox potential for Co/Co²⁺ (−0.28 V *vs.* SHE) is much lower than those for both PtCl$_4^{2+}$/Pt (0.76 V *vs.* SHE) and Cu⁺/Cu (0.52 V *vs.* SHE) and therefore the seeding Co from the ablated target is anticipated to go through GRR with both the metal precursor salts (K_2PtCl_4 and CuCl) during the process. By changing the initial K_2PtCl_4 and CuCl salt concentrations, solution phase pH, and ablation time, PtCuCo ternary NAs with various elemental ratios were synthesized *via* LASiS-GRR. Beyond the PtCuCo NAs, the design of three other ternary NAs is reported here, namely, PtRu(Ni), PtCo(Mn) and PtNi(Ti) where the bracketed elements indicate the target metals being ablated that have the desired redox potential gaps from the two respective precursor salts in each case. To this end, the relative redox potential gaps between the various transition metals and the metal salts are summarized in Table S4 in the ESI.† In addition to this, Table S3† also provides the detailed protocols for the HCl wash used to dissolve the superfluous target metal oxides from each of the aforesaid samples. It was observed from our experiments that cobalt oxides (CoO/Co_3O_4) exhibit the highest solubility in HCl, followed by CuO/Cu_2O, MnO and NiO, while TiO_2 remained almost insoluble.

2.2 Characterization

A Zeiss Libra 200MC monochromated transmission electron microscope (TEM) was used with an accelerating voltage of 200 kV for regular TEM characterization along with selected area electron diffraction (SAED) and energy-dispersive X-ray spectroscopy (EDX). A Zetasizer (Malvern, Nano ZS) was used for measuring the zeta potentials of the colloidal solutions. Inductively coupled plasma optical emission spectroscopy (ICP-OES) (Perkin Elmer, Optima 4300 DV) was performed to measure the % atomic concentrations/ratios for all the elements (Pt, Cu, Co, Ni, Mn) under study, where standard $CoCl_2$, $NiCl_2$, $MnCl_2$, CuCl and K_2PtCl_4 solutions (all ≥99.9%) were used for the calibrations. X-ray diffraction (XRD) was carried out on a Philips X'Pert-Pro diffractometer equipped with a Cu Kα source at 45 kV and 40 mA. The mean crystal sizes of the NAs were determined from XRD measurements based on the Scherrer equation:

$$d = \frac{0.9\lambda}{\beta \cos\theta}$$

where d is the mean crystal size, λ is the wavelength of the X-ray, β is the line broadening at half the maximum intensity (FWHM), and θ is the Bragg angle.

X-ray photoelectron spectroscopy (XPS) data was collected using a PHI 3056 spectrometer with an Al anode source operated at 15 kV and an applied power of 350 W. The lowest-energy carbon peak was used to calibrate the binding energy shifts of the samples (C 1s = 284.8 eV) which were typically 0.1 eV. High-resolution data was collected at a pass energy of 23.5 eV with 0.05 eV step sizes and a minimum of 60 scans was acquired to improve the signal-to-noise ratio.

2.3 Electrochemical tests

The rotating disk electrode (RDE) setup (maker: Pine Instrument Company, LLC) includes a conventional, three-compartment electrochemical cell composed of a saturated double junction Ag/AgCl electrode as the reference electrode, a glassy carbon RDE with a diameter of 5 mm as the working electrode, and a platinum coil as the counter electrode. All electrochemical (EC) tests were carried out at room temperature in 0.1 M $HClO_4$ solution with the reference electrode

Table 1 Summary of the synthesis parameters as well as the resultant mean crystal size (from XRD), zeta potential (ZP, from DLS) and elemental ratios (from ICP-OES) for the ternary NAs under study

	pH	K_2PtCl_4 (mM)	CuCl (mM)	Ablation time/min	Pt%	Co%	Cu%	Mean size/nm	ZP/mV
PtCo	pH 7	0.3	0	6	80	20	0	6.17	−43.40
PtCuCo-1			0.08		74	16	10	6.04	−44.50
PtCuCo-2			0.16		72	12	16	6.09	−42.10
PtCuCo-3			0.48		71	11	18	6.31	−41.50
PtCuCo-4	pH 11		0.3	10	62	17	21	5.80	−47.20

2076 | *Catal. Sci. Technol.*, 2017, **7**, 2074–2086

This journal is © The Royal Society of Chemistry 2017

calibrated with respect to the reversible hydrogen electrode (RHE). 20% Pt/C from BASF was used as the standard catalyst for all comparisons. For the ORR tests, synthesized nanoalloys (NAs) were probe-sonicated in ethanol first then mixed with Vulcan XC-72R carbon black (CB) powder (fluffy form, procured from Cabot Company) in ethanol with a weight ratio of 1 : 3 (NA : CB). After 30 min of mild ultrasonication, the slurry was stirred for 24 hours and then completely dried under vacuum at 80 °C for 10 hours. Thereafter, the catalyst ink was prepared by suspending 1 mg of the dried mixture in 0.5 mL of ethanol and 5 μL of 5 wt% Nafion solution (Sigma-Aldrich, density = 0.874 g mL^{-1}) via 10 min of ultrasonication. For preparing the working electrode, the rotational drying method was applied. Specifically, 10 μL of the prepared catalyst ink was drop casted onto the surface of the glassy carbon electrode (GCE) that was loaded upside down in the RDE setup and rotated at 600 rpm for 5 min. The total NP loading density was calculated to be 25 μg cm^{-2}. Cyclic voltammetry was conducted over a potential range from +0.05 V to +1.00 V at a scan rate of 100 mV s^{-1} after pre-scanning with the same potential range for 40 cycles. The ORR polarization curves were obtained at a scan rate of 5 mV s^{-1} and a rotation rate of 1600 rpm. The stability tests were carried out by recording the RDE curves after cycling at 400 mV s^{-1} for 2000 and 4000 cycles.

3. Results and discussion

3.1 PtCuCo ternary NAs

The NA samples of primary interest, as listed in Table 1, are denoted as PtCo and PtCuCo-1, 2, 3 or 4, with the detailed synthesis parameters, percentage (atomic ratio) compositions

(measured via ICP-OES), crystal sizes (calculated from XRD patterns) and zeta potentials. The TEM image in Fig. 1a reveals one of the products (PtCuCo-2) to have spherical shaped particles with no severe agglomeration, which can be attributed to the plasma-induced Stern layer negative surface charges (~−43 to −47 mV) indicated by the zeta potential measurements (see Table 1 where the onset zeta potential for agglomeration is typically reported to be around −35 mV).[73,74] The enlarged TEM image along with the corresponding particle size distribution (as averaged over three different areas) is provided in the ESI† (Fig. S3). The mean particle size from these images is roughly calculated to be around 10 nm, which could be larger than the real value due to the lack of visual resolution to accurately count extremely small NPs (<3 nm). As a consequence, the following paper used crystal sizes measured from XRD as the reference frame for size comparisons. A typical face-centered cubic (FCC) crystalline structure is demonstrated by the selected area electron diffraction (SAED) pattern in Fig. 1d, which can be assigned to the Pt-based alloy by comparing the diffraction ring diameters that indicate 2/d-spacing similar to the standard values of the Pt lattice planes. EDX mappings of the three elements, $i.e.$ Pt, Cu and Co in Fig. 1c, e and f respectively corresponding to the high-angle annular dark-field (HAADF) image in Fig. 1b, indicate a uniform distribution of all the three elements on most of the particles. These results corroborate that the NPs produced are mainly composed of PtCuCo ternary NAs with no residual metal oxides that are successfully washed away by suitable acid treatments as indicated in the synthesis steps earlier. The elemental ratios and crystal sizes for the five as-synthesized NAs can be seen in Table 1, while Fig. 2
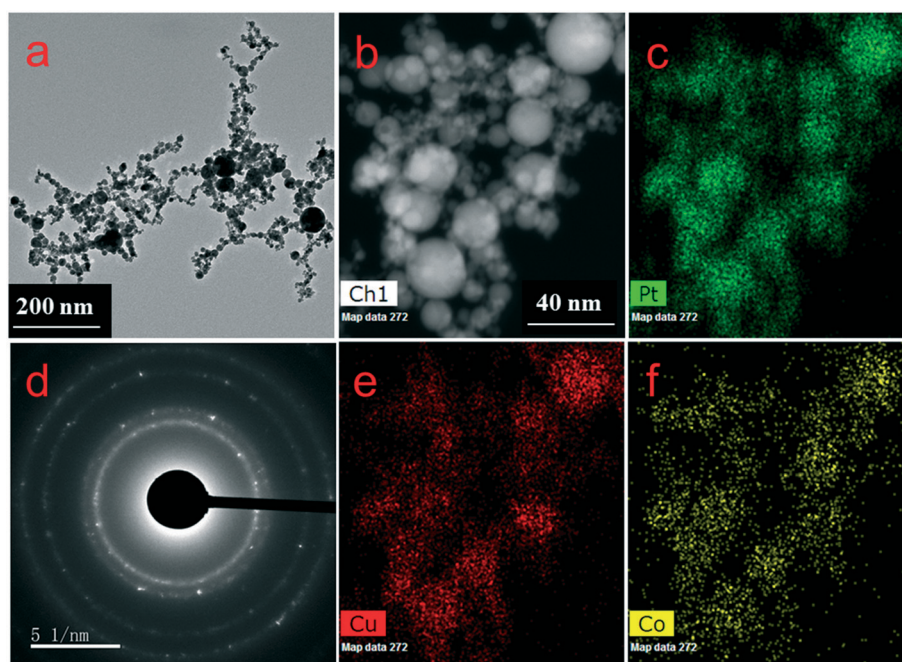

Fig. 1 Detailed structural characterization of PtCuCo-2 NAs indicating: a. TEM image; b. high-angle annular dark-field (HAADF) scanning TEM image; d. the corresponding SAED pattern for the NA samples shown in (a); c, e, f. the corresponding Pt, Cu and Co mappings from EDX analysis for (b).
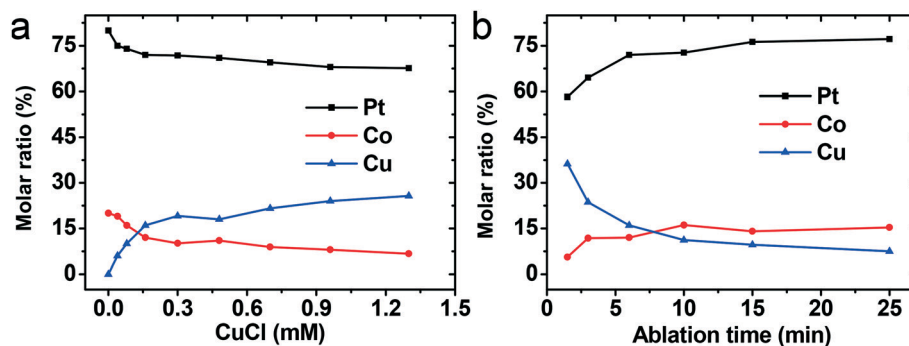
This journal is © The Royal Society of Chemistry 2017

$Catal. Sci. Technol.$, 2017, **7**, 2074–2086 | **2077**

Fig. 2 ICP-OES measurements to study the variations of the elemental ratios (molar ratio (%) for Pt, Co and Cu) in PtCuCo ternary NAs synthesized *via* LASiS-GRR: a. with different initial [CuCl] (initial [K_2PtCl_4] = 0.3 mM, ablation for 6 min); b. with different ablation times (initial [K_2PtCl_4] = 0.3 mM, [CuCl] = 0.16 mM).

provides a more systematic comparison of the component atomic elemental ratios *versus* the initial [CuCl] (Fig. 2a) and ablation times (Fig. 2b). Under the pH 7 conditions, increasing the initial [CuCl] while keeping [K_2PtCl_4] at a constant value (0.3 mM) results in dramatic reductions of the resultant Pt% and Co% at first, which are compensated by the upsurge of Cu%. However, when the initial [CuCl] rises up to over 0.16 mM, the elemental substitution rates go down gradually, indicating a point where the GRR between the reduced Cu and the remaining K_2PtCl_4, *i.e.*, $PtCl_4^{2+}$ + Cu(reduced) → Pt + Cu^{2+}, is also facilitated and in turn retards the rate of increase in Cu%. In fact, this phenomenon can be regarded as a de-alloying process, and is further corroborated by Fig. 2b, where the Co% remains almost constant, while the Cu atoms are gradually replaced by Pt in the NAs during ablation as a result of the aforementioned GRR process. It needs to be pointed out that the PtCuCo-4 NAs were synthesized under alkaline conditions (pH 11) in which case the atomic Pt% is further reduced to 62% while both Co and Cu atomic ratios are higher than those for the NAs synthesized under the pH 7 conditions (see Fig. S4† for the detailed EDX mapping). The abovementioned results from our synthesis processes can be easily rationalized by the fact that seeding Co NPs go through the following series of competing reactions during the ultrasonic quenching of the LASiS-GRR process:
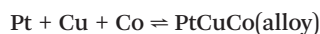
1. GRR with either Pt or Cu precursor salts,

$$PtCl_4^{2+} + Co → Pt + Co^{2+}$$

$$2Cu^+ + Co → 2Cu + Co^{2+}$$
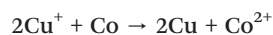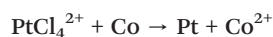
2. Oxidation by water (solution phase H^+) driven by pH,

$$Co + 2H_2O \rightleftharpoons Co^{2+} + 2OH^- + H_2$$

3. Alloying with reduced Pt and Cu,

$$Pt + Cu + Co \rightleftharpoons PtCuCo(alloy)$$

With respect to the aforementioned reaction pathways, one can easily observe that the alkaline conditions will largely slow down the second reaction, *i.e.*, direct oxidation of seeding Co NPs in water which, in turn, makes more Co available for alloying with reduced Pt and Cu.

The alloying between Pt, Cu, and Co is further characterized by XRD as shown in Fig. 3. All samples exhibit clear peak shifts to higher angles in regard to pure Pt, as shown by the dashed lines. This according to Bragg's law indicates reduction of the Pt lattice constant which is ascribed to the atomic overlaps against Cu and Co atoms that have smaller lattice constants. It can be seen from Fig. 3 that all four pH 7 NA samples exhibit comparable positive Pt (111) peak shifts of around 0.45° (see Table S1 in the ESI†). One needs to bear in mind that the lattice constant for Cu is 3.61 Å, which is relatively closer to that for Pt (3.92 Å) and slightly larger than that for the FCC structures of Co (3.55 Å). Thus, although the Pt% declines with increasing initial [CuCl], the higher Cu% in the NAs results in similar lattice shrinkage for PtCuCo-1, 2 and 3. On the other hand, the XRD data for the PtCuCo-4 sample demonstrate a more distinct Pt (111) peak shift to 40.5° (in comparison with the pure Pt (111)
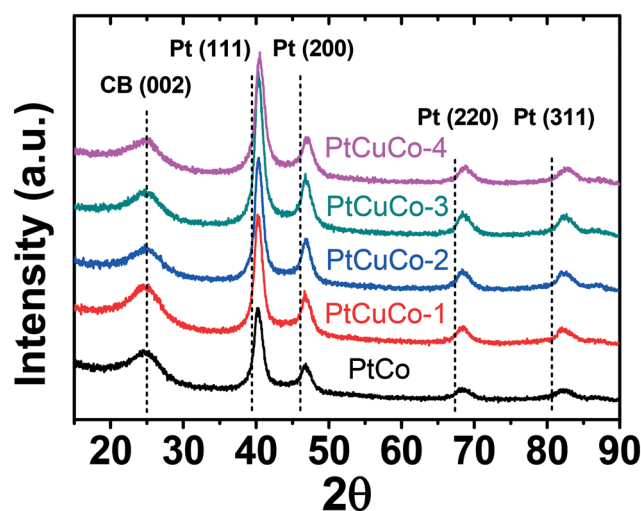

Fig. 3 XRD patterns of the PtCo NA and the four PtCuCo ternary NA (PtCuCo-1, 2, 3, 4) samples investigated in this study. The dashed lines represent the standard peak positions for Pt (111), Pt (200), Pt (220) and Pt (311) facets.

2078 | *Catal. Sci. Technol.*, 2017, **7**, 2074–2086

This journal is © The Royal Society of Chemistry 2017

peak at 39.8°), which corroborates the ICP results for a larger degree of alloying under alkaline conditions. Besides, the mean crystal size for each sample is also calculated from the FWHM of the Pt (111) peak (as described in the Experimental details) and is found to be largely influenced by the K_2PtCl_4 concentration and the ablation time. In fact, the increase in both [K_2PtCl_4] and ablation time favor NA nucleation and growth, therefore improving the crystal size, as shown in Table S2† and demonstrated by our earlier studies.[44] In contrast, the impact of the variations in [CuCl] on the NA sizes is found to be minor due to the lower redox potential of Cu/Cu$^+$ (0.52 V vs. SHE) resulting in a smaller atomic ratio in the NAs. As revealed by Table 1, all the PtCo and PtCuCo samples with the same [K_2PtCl_4] and ablation time but different initial CuCl concentrations exhibit similar crystal sizes (~6 nm). However, with longer ablation time, the NA samples made under pH 11 conditions (PtCuCo-4) show a slightly smaller mean size (~5.80 nm) than those made under pH 7 conditions. This is largely attributed to the initial formation of Pt(OH)$_2$ and CuOH that in fact reduces the precursor salt concentrations.

In order to further investigate the detailed elemental distributions inside the synthesized NAs, a line scan across the center of the EDX mapping on an enlarged isolated particle of PtCuCo-2 was conducted. As shown in Fig. 4, the elemental ratio profiles clearly indicate the particle to be composed of a Pt and Cu-enriched (more Pt and medium Cu) shell ~1–2 nanometers in size along with a relatively uniform PtCuCo alloyed core. The detection of such a shell–core structure is consistent with our earlier work on the PtCo binary NA, where a Pt-rich shell was also found using electron energy loss spectroscopy (EELS) mapping.[44] The uneven elemental distribution on the shell is driven by both the de-alloying pro-

cess that is controlled by the respective redox potentials and the acid leaching process driven by the reactivity/solubility of each metal and/or the corresponding oxide in HCl acid (see Tables S4 and S5† for the detailed redox potential and solubility values). Such relative gradients/gaps in redox potentials/solubility act as the driving force for the component elements to segregate out of the NAs in varying rates, thereby leading to the formation of a shell with mostly Pt (most inert and least soluble), minor Cu (medium active and soluble) and little Co (most active and soluble). It needs to be pointed out that this Pt-rich shell nanostructure is well known to benefit the ORR catalysis.

Finally, XPS was performed to investigate the shifts of electron binding energy (E_{be}) for the PtCo, PtCuCo-2, and PtCuCo-4 samples. As shown in Fig. 5a–c, the Pt 4f peaks indicate a positive binding energy shift compared to those of pure Pt (depicted by the dashed lines). However, with the increase of Cu%, the Pt $4f_{7/2}$ binding energy gradually shifts back from 71.81 eV for PtCo NA to 71.66 eV for PtCuCo-2 and 71.62 eV for PtCuCo-4 NAs. Similar reductions in binding energies are also seen for other Pt peaks, i.e., the Pt $4f_{5/2}$ binding energy drops from 75.13 to 74.98 and 74.93 eV, while the Pt $5d_{5/2}$ binding energy peak downshifts from 315.71 to 315.58 and 315.50 eV for the PtCo, PtCuCo-2 and PtCuCo-4 samples, respectively (refer to Fig. S6 in the ESI†). As mentioned earlier in the introduction, Cu is located to the right of Pt in the periodic table and has a slightly higher d-band center than Pt, in contrast to the lower d-band center of Co. As a consequence, alloying Pt with Cu is expected to shift the d-band center up and lower the E_{be}, while alloying with Co will downshift the Pt d-band and improve the E_{be}. This will be further discussed later when correlating these shifts to the affinity of oxygen/oxygenated species on catalyst surfaces to
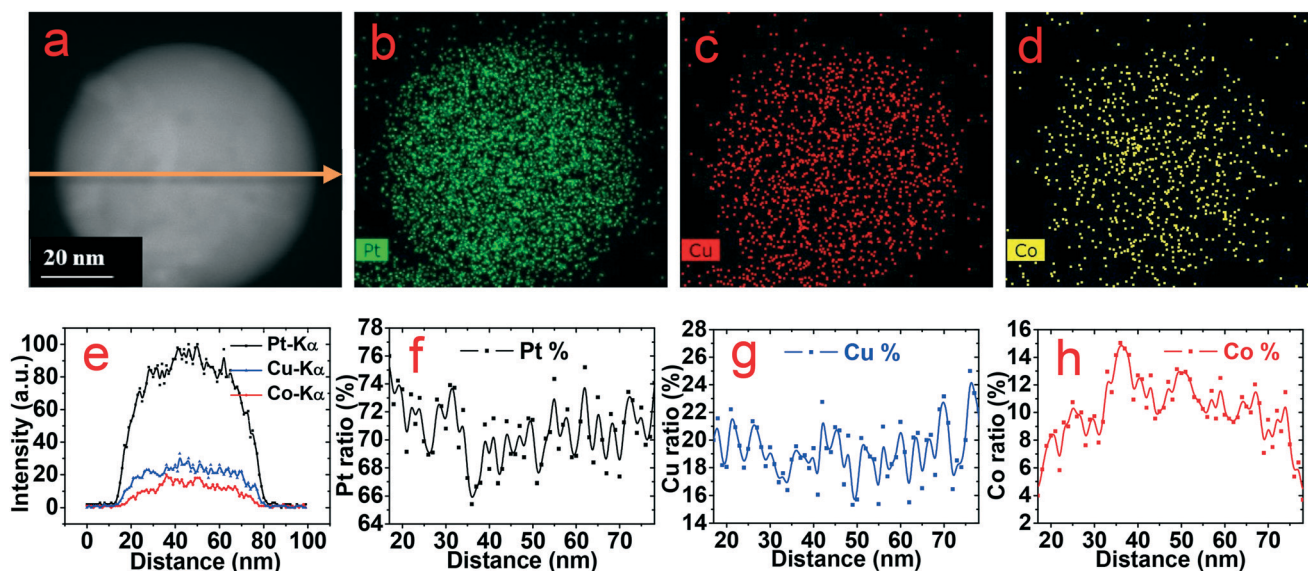

Fig. 4 EDX elemental mappings and line scans for an enlarged image of an isolated PtCuCo-2 particle indicating: a. HAADF image, where the yellow arrow represents the line scan position and direction; b–d. the corresponding EDX mappings; e. the corresponding line scans for Pt, Cu and Co from (a); f–h. the calculated elemental ratios across the line scan for Pt (f), Cu (g) and Co (h).
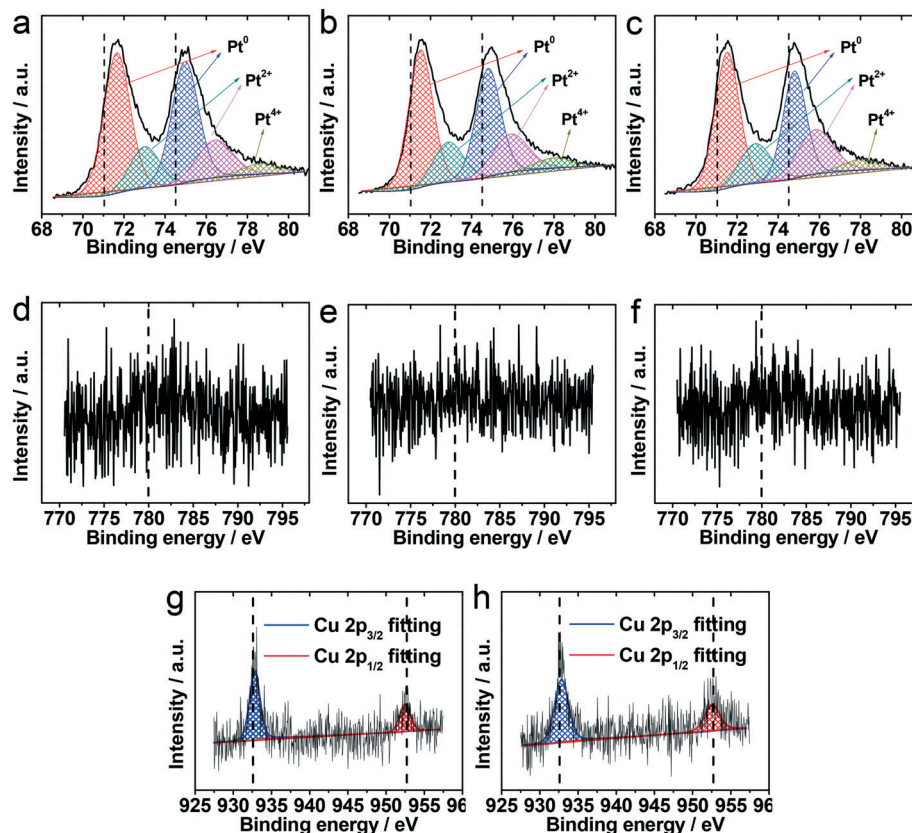
This journal is © The Royal Society of Chemistry 2017

Catal. Sci. Technol., 2017, **7**, 2074–2086 | **2079**

Fig. 5 XPS spectra indicating the peaks of Pt 4f$_{7/2,5/2}$ (a–c), Co 2p$_{3/2}$ (d–f), and Cu 2p$_{3/2}$ (g and h) for: (a and d) PtCo-1; (b, e and g) PtCuCo-2; (c, f and h) PtCuCo-4 NAs. The dashed lines demonstrate standard peak positions for the respective species.

rationalize their catalytic activities. Besides, the XPS results also qualitatively reveal the surface elemental compositions of a few atomic layers. Weak Co 2p$_{3/2}$ peaks are found for all three samples, while Cu 2p$_{3/2}$ peaks exhibiting higher intensities are found for the two PtCuCo NAs, with PtCuCo-4 showing a slightly higher surface Cu ratio after normalizing by the Pt peak area at the same signal-to-noise ratio. This corroborates our earlier elemental ratio results as well as the proposed core–shell structure with a Pt and Cu-enriched shell.

The ORR catalytic activities of the synthesized PtCuCo NAs (PtCuCo-1, 2, 3, 4) were investigated and compared with those of both commercial Pt/C and the binary PtCo NA catalysts. As shown in Fig. 6, the electrochemical surface area (ECSA) of the NA catalysts is determined from the broad peaks located between 0.05 and ~0.3 V representing H$_2$ adsorption (forward scan) and desorption (back scan) in the cyclic voltammetry (CV) plots. The CV scans clearly indicate that with the increase of Cu%, the ECSA slightly improves for PtCuCo-1, whereas it is gradually reduced for the PtCuCo-2 and PtCuCo-3 samples. It is well known that Pt atoms are the most active for H$_2$ evolution, therefore the addition of surface Cu presumably lowers the ECSA for PtCuCo-3 and 4. The initial minor increase in ECSA for the PtCuCo-1 case is probably due to the further lattice shrinkage, while the minimal amount of atomic Cu (10% at. as seen in Table 1) renders the

surface Cu% even lower and hence barely affects the active surface area. The ORR polarization curves shown in Fig. 6b indicate that all four aforementioned NAs exhibit earlier half-wave potentials and therefore lower overpotentials than the commercial Pt/C (details seen from the inset in Fig. 6b). It is also clearly observed that the PtCuCo-2 sample shows the best performance in terms of half-wave potential and overpotential, with values of ~0.905 V and 0.325 V, respectively. Fig. 6c indicates the Tafel slopes for all the synthesized samples to be between 60–65 mV dec^{-1} as compared to the corresponding value of ~71 mV dec^{-1} for commercial Pt/C. This, in turn, implies better charge carrier mobility for the synthesized catalysts. Mass (MA) and specific (SA) ORR activities (obtained by normalizing the kinetic current densities at 0.9 V $vs.$ RHE by Pt loading and ECSA, respectively), as extracted from the Tafel plots, are also summarized in Table 2. Clearly, the PtCuCo-2 NA sample exhibits the best catalytic activities with a 4- and 6.5-fold increase in MA (0.32 A mg^{-1}) and SA (1.4 mA cm^{-2}), respectively, as compared to the values for commercial Pt/C (0.08 A mg^{-1} and 0.22 mA cm^{-2}). It should be noted that detailed calculations and results from Koutecky–Levich analysis on rotating disk voltammetry data at different rotation speeds indicate an ideal complete four-electron transfer process for the ORR activities (shown in Fig. S8 in the ESI†).
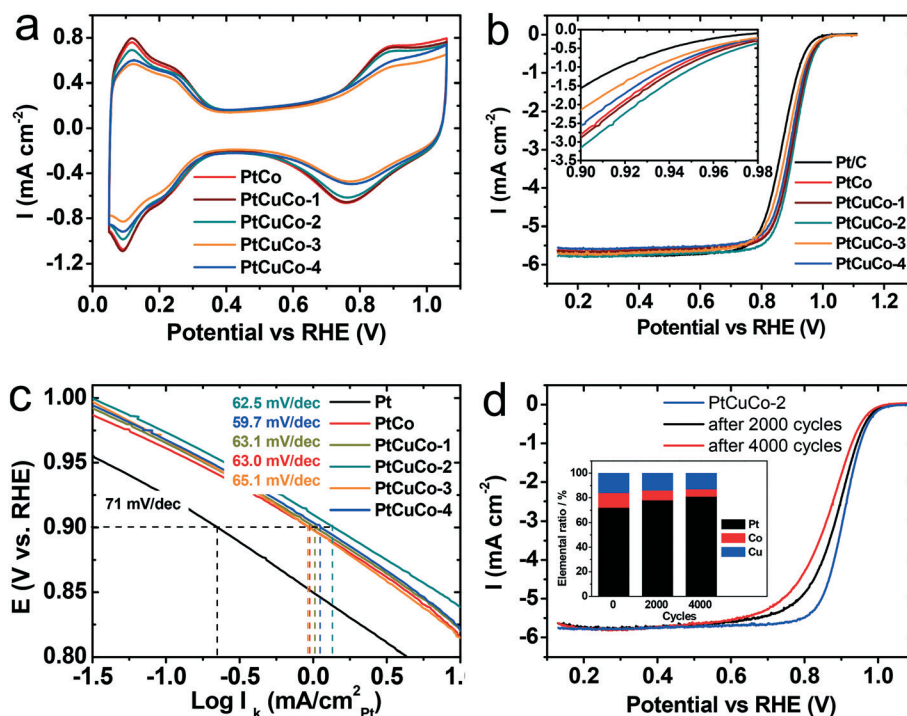
2080 | Catal. Sci. Technol., 2017, 7, 2074–2086

This journal is © The Royal Society of Chemistry 2017

Fig. 6 Electrochemistry data indicating the ORR activities of PtCo and PtCuCo ternary NAs made *via* LASiS-GRR, as compared to commercial Pt/C samples, using: a. cyclic voltammetry curves at a scan rate of 100 mV s^{-1}; b. ORR polarization curves at 1600 rpm and a scan rate of 5 mV s^{-1}; c. the corresponding Tafel plots for the kinetic part of the current from (b); d. ORR polarization curves as well as the component elemental ratios in the PtCuCo alloy (shown in the inset) after 2000 and 4000 CV scans.

The overall superior ORR activities of all the synthesized NA catalysts are largely attributed to the surfactant-free synthesis technique (LASiS-GRR) that produces core–shell nanostructures with a Pt-rich shell and meanwhile does not warrant the use of unwanted surfactant/ligands that are known to impede the interfacial catalytic sites. Specifically, the best ORR activity of PtCuCo-2 is ascribed to the moderate NA sizes (~6 nm) as well as the optimized binding affinities for both oxygen and oxygenated species, which is also corroborated by the binding energy shifts of Pt (71.66 eV) for Pt $4f_{7/2}$ from the XPS results in Fig. 5b. As shown in Fig. 7, the electron binding energy (E_{be}, eV) from the XPS measurements qualitatively refers to the energy difference between the Pt(Cu)(Co) d-band center (E_{dbc}) and the nucleus. On the other hand, Pt–O/OH binding affinities can be inferred from the energy gaps between E_{dbc} and the Fermi energy levels E_F (located within the antibonding orbital for the metal adsorbate *i.e.*, Pt–O/OH interactions). Clearly, a smaller energy gap translates to stron-

ger binding affinity. Thus, a larger E_{be} from the XPS measurements (implying a smaller energy difference between the d-band center and the nucleus) translates into a downshift of the E_{dbc} levels which, in turn, implies a weaker binding affinity for the Pt–O/OH interactions owing to the larger energy gap of ($E_{dbc} - E_F$). Pt metal by itself has a relatively lower E_{be} (~71 eV), therefore a higher E_{dbc} level and stronger binding affinity towards oxygenated species. This poses an obstacle for desorbing the species from the catalyst surface that eventually can block the catalytically active surface sites. To this end, alloying Pt with Co effectively increases the E_{be} (revealed from the XPS results in Fig. 5a), thereby lowering the E_{dbc} and, in turn, facilitating the easier desorption of oxygenated species from catalyst surfaces through weakened binding affinities. However, in such case, the concurrently reduced oxygen affinity might also relatively slow down the oxygen adsorption process, thereby hindering the catalytic performance. We address this by optimal tuning of the surface

Table 2 Summary of the electrochemical test results for the PtCo NAs and PtCuCo ternary NAs under study as compared to the results for standard Pt NPs

	Charge (mC)	Pt wt%	Pt loading (μg cm^{-2})	ECSA (m^2 g^{-1})	I_k at 0.9 V (mA cm^{-2})	MA (A mg^{-1})	SA (mA cm^{-2})
Pt	0.396	100.0	25.00	38.42	2.11	0.08	0.22
PtCo	0.259	93.0	23.24	25.13	5.55	0.24	0.95
PtCuCo-1	0.260	90.1	22.53	25.22	5.77	0.26	1.02
PtCuCo-2	0.237	89.0	22.25	22.99	7.15	0.32	1.40
PtCuCo-3	0.186	88.5	22.13	18.04	3.43	0.16	0.86
PtCuCo-4	0.202	83.7	20.93	19.60	4.64	0.22	1.13

This journal is © The Royal Society of Chemistry 2017

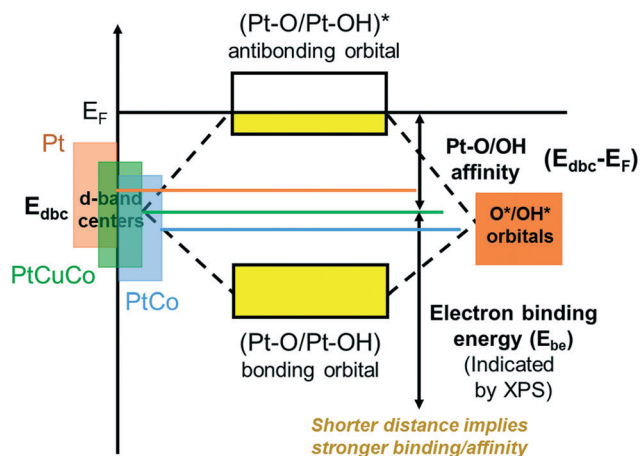*Catal. Sci. Technol.*, 2017, **7**, 2074–2086 | **2081**

Fig. 7 Schematic diagram indicating the role of d-band center positions for Pt(Cu)(Co) NAs in driving the electron binding energy (estimated from XPS) and Pt–O/OH binding affinity.

electronic structures of our catalysts through directed alloying of Pt and Co with a third transition metal Cu in a fashion that results in balancing both the aforementioned affinities. The rationale behind our catalyst design here is that the slight decrease in Pt electron binding energy ($\sim$71.66 eV) in the PtCuCo NAs compared to that of the PtCo NA ($\sim$71.81 eV), as confirmed by the XPS results in Fig. 5a–c, implies an upshifting of its d-band from that of the PtCo NA. In turn, this does not impair the interfacial oxygen adsorption process while promoting the easy removal of oxygenated species from the catalyst surface. In line with this rationale, the PtCuCo-3 and 4 samples clearly show a decline in their ORR activities which can be attributed to the large binding energy back shifts for Pt that binds the oxygen too strongly and severely hinders its desorption processes. We conclude our catalytic measurements with the stability test conducted for PtCuCo-2. As seen from Fig. 6d, after 2000 and 4000 CV scans, the catalytic activity does exhibit a gradual but not severe decline which is a well-known phenomenon due to the dissolution of the catalysts in the electrolyte. Upon detailed analysis, one can observe that the initial elemental ratios of Pt : Co : Cu change from 72 : 12 : 16 to 78 : 8 : 14 (after 2000 cycles) and 81 : 6 : 13 (after 4000 cycles). This can be readily explained from the higher solubility/reactivity of Co in the acid as compared to Cu and Pt. It needs to be pointed out that the reported LASiS-GRR here does not involve any post-annealing steps, which we propose to apply in our future research efforts to initiate ordered NA formation. Our hypothesis is that such ordered nano-alloyed structures can prevent the leaching of constituent elements, thereby increasing the stability of the aforementioned ORR catalysts during their operation.

3.2 Tuning NA structure and composition: the mechanistic picture and impact of experimental parameters

The proposed LASiS-GRR technique has provided a facile route for the synthesis of surfactant-free binary PtCo and ter-

nary PtCuCo NAs whose ORR activities can be designed with tailored size and elemental ratios/distributions *via* direct tuning of the initial metal salt concentrations, ablation time, laser fluence (LF) and solution phase pH. To this end, we describe the mechanistic picture behind the operation of the LASiS-GRR technique in Fig. 8 which schematically presents the diverse sizes (represented by the size of circles) and compositions (represented by the colour pie-chart in the circles) of the PtCuCo NAs synthesized under different operating conditions. As discussed in the introduction and based on previous studies,[51–55] ions/solutes in solution can also be contained in the early stage of cavitation bubbles to initiate the GRR process simultaneously with plasma quenching and nucleation. Specifically, with higher initial $[PtCl_4^{2-}]$ and longer ablation time, NAs with larger sizes and lower alloying ratios are formed, as seen in Fig. 2b and S9a and Table S2 in the ESI.† The former is due to the higher rates of particle nucleation and Ostwald ripening, while the latter is ascribed to the remaining $PtCl_4^{2-}$ salts de-alloying the already formed surface Co and Cu atoms (as also discussed earlier in Fig. 2b). Similarly, a wide range of sizes and alloying can be tailored through the combination of the use of low/medium $PtCl_4^{2-}$ salt concentrations and/or short/medium durations of laser ablation. On the other hand, by changing the $[Cu^+]$, the component elemental ratios can also be rationally tuned, in which case a higher $[Cu^+]$ leads to more Pt and Co atoms to be displaced by Cu in the NAs without affecting the particle sizes (as also discussed earlier in Fig. 2a). Furthermore, our results indicate that changing the pH to mildly alkaline (pH 11) conditions causes more Co to go through GRR instead of being oxidized directly by water. This results in a high alloying ratio but a relatively smaller particle size. Finally, the impact of laser fluence (LF) on the resultant alloying ratios and crystalline sizes was also investigated in this study with the results summarized in Fig. S9b and Table S2 in the ESI.† It needs to be mentioned here that the first three lower LFs were achieved using unfocused laser beams by simply adjusting the laser Q-switch delay time, where the increase of LF directly enhances the seeding [Co] production rate. This results in a higher Co ratio (%) in the products, which can be interpreted as equivalent effects of lowering the initial $[PtCl_4^{2-}]$ and inducing a smaller $[PtCl_4^{2-}]/[Co]$ ratio. However, the high [Co] concentrations emerging from the LASiS, and consequent fast $PtCl_4^{2-}$ reduction rates, also promote the Pt nucleation rates which results in relatively larger particle sizes. The three higher LFs were tuned using focused lasers, in which case the absolute [Co] production rates largely become a function of the focused ablation area with weak dependence on the laser fluence. As a consequence, the resultant alloying ratios and particle sizes do not indicate any drastic change. Such systematic studies on the directed control of the LASiS-GRR protocols to drive desired nanoparticle sizes and extent of alloying allow us to investigate the inherent relationships between elemental compositions and subsequent Pt binding energy/d-band center shifts with respect to the catalytic activities of a wide class of ternary NAs. Our
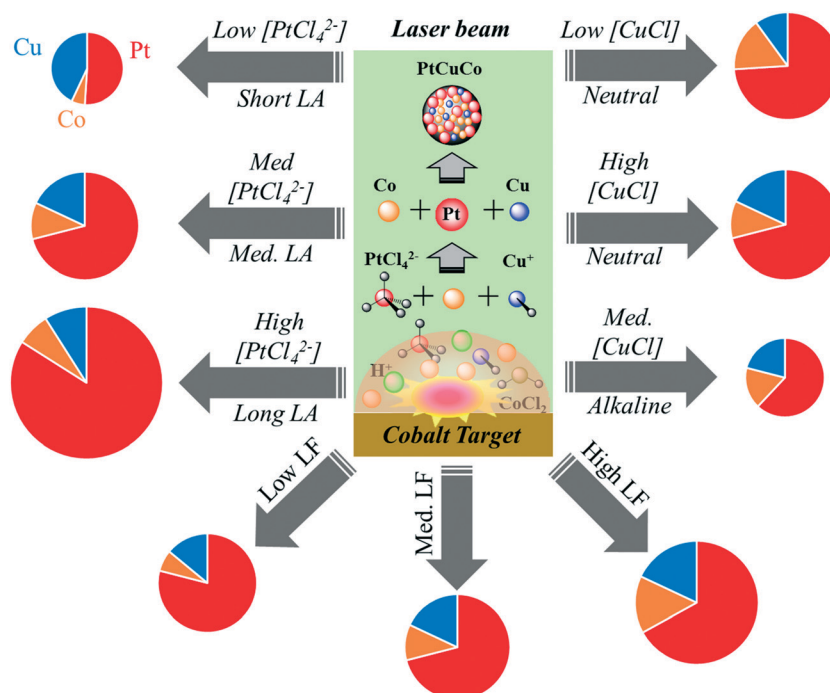
2082 | *Catal. Sci. Technol.*, 2017, **7**, 2074–2086

This journal is © The Royal Society of Chemistry 2017

Fig. 8 Schematic diagram depicting the mechanistic picture behind the formation of PtCuCo ternary NAs with various particle sizes (size of circles) and elemental compositions and distributions (colored pie-charts in the circles) *via* LASiS-GRR by using different initial salt concentrations, ablation times, laser fluences (LF) and pH conditions.

ongoing research efforts are aimed toward carrying out molecular dynamics (MD) and kinetic Monte Carlo (KMC) simulations to mimic the LASiS-GRR process. By combining them with the current experimental results as well as *in situ* diagnostic techniques, we hope to unveil the mechanistic picture of the LASiS-GRR technique at a molecular level. Such studies will provide detailed fundamental understanding in regard to the aforementioned impacts of laser/environmental parame-

ters on the nucleation and alloying/dealloying behaviours, and thereby the resultant particle sizes and component ratios of the as-synthesized nanoparticles.

3.3 Other ternary NAs

In our final effort towards establishing the potential of the LASiS-GRR technique to rapidly screen wide classes of
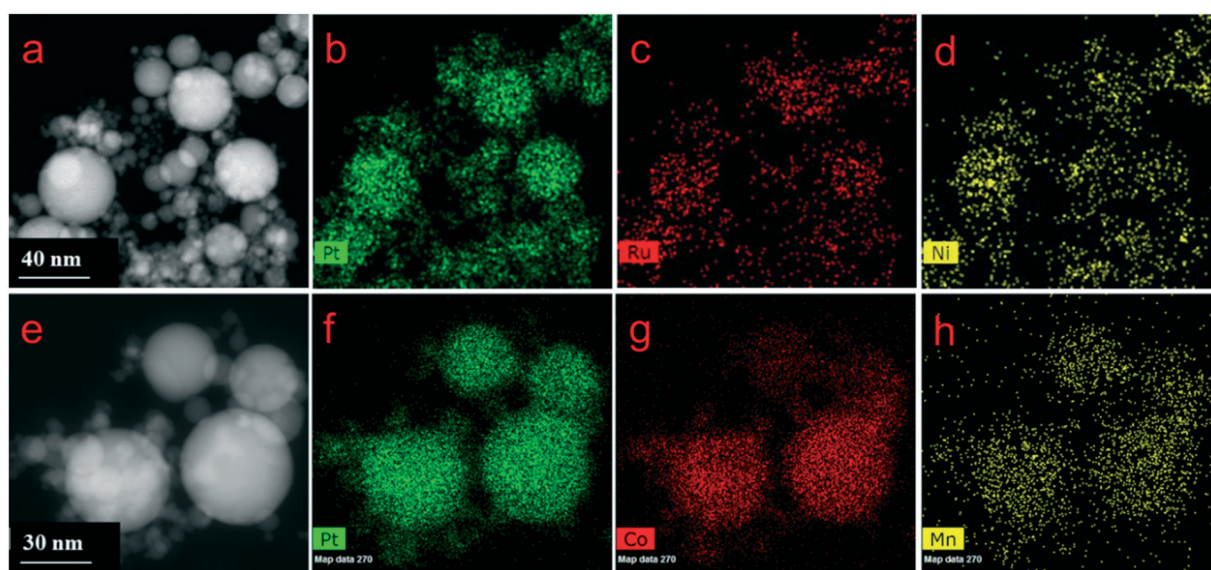

Fig. 9 HAADF images and the corresponding EDX elemental mappings indicating the formation of PtRuNi (a–d) and PtCoMn (e–h) ternary NAs synthesized *via* LASiS-GRR.
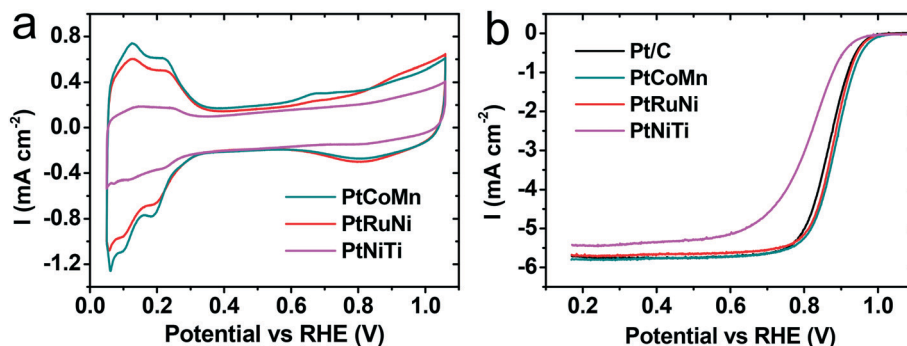
This journal is © The Royal Society of Chemistry 2017

Catal. Sci. Technol., 2017, **7**, 2074–2086 | **2083**

Fig. 10 Electrochemical data for the other Pt-based ternary NAs (namely, PtRuNi, PtCoMn and PtNiTi) made by LASiS-GRR showing: a. cyclic voltammetry curves at a scan rate of 100 mV s^{-1}; b. ORR polarization curves at 1600 rpm and a scan rate of 5 mV s^{-1}.

Table 3 Summary of electrochemical test results for the other Pt-based ternary NAs under study

	Charge (mC)	Pt wt%	Pt loading (μg cm^{-2})	ECSA (m^2 g^{-1})	I_k at 0.9 V (mA cm^{-2})	MA (A mg^{-1})	SA (mA cm^{-2})
Pt	0.40	100.0	25.00	38.42	2.11	0.08	0.22
PtCoMn	0.243	81.3	20.33	23.57	3.67	0.18	0.77
PtRuNi	0.199	86.5	21.63	19.30	2.78	0.13	0.67
PtNiTi	0.053	72.1	18.03	5.14	0.61	0.03	0.66

intermetallic nanocatalysts, we have also extended the technique to the synthesis of other Pt-based ternary NAs such as PtRu(Ni), PtCo(Mn) and PtNi(Ti). Here, two critical factors need to be taken into consideration for choosing the suitable elemental combinations, namely, matching of redox potential gradients and the target metal/metal oxide solubility in the acid used in the washing step, as discussed in detail in the ESI.† The EDX elemental mapping results based on the HAADF images in Fig. 9 indicate uniform elemental distributions for the successfully synthesized PtRuNi and PtCoMn ternary NAs. However, the PtNiTi ternary NAs synthesized are mostly covered by a TiO$_2$ shell (see Fig. S10 in the ESI†) due to the extremely low solubility of TiO$_2$ in acids. The ORR catalytic activities of the above three ternary NAs are also compared in Fig. 10 and Table 3. As seen from Fig. 10, both the PtRuNi and PtCoMn NAs exhibited earlier half-wave potentials and therefore lower overpotentials than the commercial Pt/C, but the PtNiTi NAs demonstrated extremely poor overpotentials and a large loss of ECSA. Although both PtRuNi and PtCoMn exhibit slightly better performances than the commercial Pt/C in terms of MA and SA (see Table 3), their activities are still weaker compared to the PtCo and PtCuCo-2 NAs. The highly retarded ORR catalytic performance of the PtNiTi NAs can be readily explained by the presence of the inert TiO$_2$ shell that largely blocks the active catalytic sites of Pt at the surface.

4. Conclusions

This work reports the use of our recently developed LASiS-GRR technique as a facile and surfactant-free route for synthesizing wide classes of Pt-based ternary NAs (including PtCuCo, PtRuNi, PtCoMn and PtNiTi) as ORR electrocatalysts.

The rational selection of elements in the catalysts designed by our synthesis approach is based on the respective target metal/metal salt relative redox potential differences, as well as the acid solubility of the target metal oxides. When compared to commercial Pt/C catalysts, the synthesized PtCuCo ternary NAs with optimally tailored crystal sizes (~6 nm) and compositions (Pt : Co : Cu ~ 72 : 12 : 16) exhibit superior ORR catalytic activities while allowing a ~28 at% reduction in Pt usage. Our results indicate that the NAs reveal a shell–core structure with the shell composed mostly of Pt and some minor amount of Cu, along with a relatively uniform PtCuCo alloyed core. The transformative concept in our LASiS-GRR technique is the ability of target-seeding NPs generated by the rate-limiting step of LASiS to drive the respective redox reactions of the rate-controlling step of GRR under non-equilibrium thermodynamic conditions at the LASiS-induced cavitation bubble–liquid interface. Such a high-energy route enables elaborate tailoring of sizes, structures and alloying/compositions of the final intermetallic nanostructures by tuning simple experimental parameters such as solution-phase salt concentration, pH, laser fluence and ablation time without using any unwanted surfactants/ligands. Moreover, the aforementioned studies have enabled us to establish the relationship between ORR electrocatalytic activities and the various structural and compositional variations in the designed nanoalloys.

Acknowledgements

2084 | *Catal. Sci. Technol.*, 2017, **7**, 2074–2086

This journal is © The Royal Society of Chemistry 2017

References

1 V. R. Stamenkovic, B. Fowler, B. S. Mun, G. Wang, P. N. Ross, C. A. Lucas and N. M. Markovic, *Science*, 2007, **315**, 493–497.

2 D. Wang, H. L. Xin, R. Hovden, H. Wang, Y. Yu, D. A. Muller, F. J. DiSalvo and H. D. Abruña, *Nat. Mater.*, 2012, **12**, 81–87.

3 M. Shao, A. Peles and K. Shoemaker, *Nano Lett.*, 2011, **11**, 3714–3719.

4 B. P. Vinayan, R. Nagar, N. Rajalakshmi and S. Ramaprabhu, *Adv. Funct. Mater.*, 2012, **22**, 3519–3526.

5 S. H. Noh, B. Han and T. Ohsaka, *Nano Res.*, 2015, **8**, 3394–3403.

6 S.-I. Choi, M. Shao, N. Lu, A. Ruditskiy, H.-C. Peng, J. Park, S. Guerrero, J. Wang, M. J. Kim and Y. Xia, *ACS Nano*, 2014, **8**, 10363–10371.

7 Y. Huang, J. Zhang, A. Kongkanand, F. T. Wagner, J. C. M. Li and J. Jorné, *J. Electrochem. Soc.*, 2014, **161**, 10–15.

8 J. Li, G. Wang, J. Wang, S. Miao, M. Wei, F. Yang and L. Yu, *Nano Res.*, 2014, 7, 1519–1527.

9 J. Greeley, I. E. L. Stephens, A. S. Bondarenko, T. P. Johansson, H. A. Hansen, T. F. Jaramillo, J. Rossmeisl, I. Chorkendorff and J. K. Nørskov, *Nat. Chem.*, 2009, **1**, 552–556.

10 V. R. Stamenkovic, B. S. Mun, M. Arenz, K. J. J. Mayrhofer, C. A. Lucas, G. F. Wang, P. N. Ross and N. M. Markovic, *Nat. Mater.*, 2007, **6**, 241–247.

11 D. Cheng, X. Qiu and H. Yu, *Phys. Chem. Chem. Phys.*, 2014, **1**, 20377–20381.

12 J.-H. Jang, E. Lee, J. Park, G. Kim, S. Hong and Y.-U. Kwon, *Sci. Rep.*, 2013, **3**, 2872.

13 A. Dutta and J. Ouyang, *ACS Catal.*, 2015, **5**, 1371–1380.

14 X. Tan, S. Prabhudev, A. Kohandehghan, D. Karpuzov, G. A. Botton and D. Mitlin, *ACS Catal.*, 2015, **5**, 1513–1524.

15 P. Zhang, X. Dai, X. Zhang, Z. Chen, Y. Yang, H. Sun, X. Wang, H. Wang, M. Wang, H. Su, D. Li, X. Li and Y. Qin, *Chem. Mater.*, 2015, **27**, 6402–6410.

16 H. Li, C. Ren, S. Xu, L. Wang, Q. Yue, R. Li, Y. Zhang, Q. Xue and J. Liu, *J. Mater. Chem. A*, 2015, **3**, 5850–5858.

17 M. A. Matin, E. Lee, H. Kim, W.-S. Yoon and Y.-U. Kwon, *J. Mater. Chem. A*, 2015, **3**, 17154–17164.

18 C. Zhang, W. Sandorf and Z. Peng, *ACS Catal.*, 2015, **5**, 2296–2300.

19 L. Liu, Z. Huang, D. Wang, R. Scholz and E. Pippel, *Nanotechnology*, 2011, **22**, 105604.

20 V. Tripkovic, H. A. Hansen, J. Rossmeisl and T. Vegge, *Phys. Chem. Chem. Phys.*, 2015, **17**, 11647–11657.

21 Y. Zhou and D. Zhang, *J. Power Sources*, 2015, **278**, 396–403.

22 Z. Zhu, Y. Zhai and S. Dong, *ACS Appl. Mater. Interfaces*, 2014, **6**, 16721–16726.

23 M. E. Scofield, C. Koenigsmann, L. Wang, H. Liu and S. S. Wong, *Energy Environ. Sci.*, 2015, **8**, 350–363.

24 J. Ryu, J. Choi, D.-H. Lim, H.-L. Seo, S.-Y. Lee, Y. Sohn, J. H. Park, J. H. Jang, H.-J. Kim, S. A. Hong, P. Kim and S. J. Yoo, *Appl. Catal., B*, 2015, **174**, 526–532.

25 M.-X. Gong, X. Jiang, T.-Y. Xue, T.-Y. Shen, L. Xu, D.-M. Sun and Y.-W. Tang, *Catal. Sci. Technol.*, 2015, **5**, 5105–5109.

26 S. Lankiang, M. Chiwata, S. Baranton, H. Uchida and C. Coutanceau, *Electrochim. Acta*, 2015, **182**, 131–142.

27 P. Mani, R. Srivastava and P. Strasser, *J. Power Sources*, 2011, **196**, 666–673.

28 J. Zhao and A. Manthiram, *Appl. Catal., B*, 2011, **101**, 660–668.

29 Y.-H. Cho, O.-H. Kim, D. Y. Chung, H. Choe, Y.-H. Cho and Y.-E. Sung, *Appl. Catal., B*, 2014, **154**, 309–315.

30 S. J. Hwang, S. J. Yoo, S. Jang, T.-H. Lim, S. A. Hong and S.-K. Kim, *J. Phys. Chem. C*, 2011, **115**, 2483–2488.

31 S.-W. Chou, J.-J. Shyue, C.-H. Chien, C.-C. Chen, Y.-Y. Chen and P.-T. Chou, *Chem. Mater.*, 2012, **24**, 2527–2533.

32 B. Li and S. H. Chan, *Int. J. Hydrogen Energy*, 2013, **38**, 3338–3345.

33 Z. Guo, X. Dai, Y. Yang, Z. Zhang, X. Zhang, S. Mi, K. Xu and Y. Li, *J. Mater. Chem. A*, 2013, **1**, 13252–13260.

34 H. Zhu, S. Zhang, S. Guo, D. Su and S. Sun, *J. Am. Chem. Soc.*, 2013, **135**, 7130–7133.

35 K. Jayasayee, J. A. R. Van Veen, T. G. Manivasagam, S. Celebi, E. J. M. Hensen and F. A. de Bruijn, *Appl. Catal., B*, 2012, **111**, 515–526.

36 M. K. Jeon and P. J. McGinn, *Electrochim. Acta*, 2012, **64**, 147–153.

37 P. Kolla and A. Smirnova, *Electrochim. Acta*, 2015, **182**, 20–30.

38 J. Li, X. Fu, Z. Mao, Y. Yang, T. Qiu and Q. Wu, *Nanoscale Res. Lett.*, 2016, **11**, 3.

39 M. Ammam and E. B. Easton, *J. Power Sources*, 2013, **236**, 311–320.

40 K. C. Neyerlin, R. Srivastava, C. Yu and P. Strasser, *J. Power Sources*, 2009, **186**, 261–267.

41 Y. Tang, F. Gao, S. Yu, Z. Li and Y. Zhao, *J. Power Sources*, 2013, **239**, 374–381.

42 J. N. Kuhn, C.-K. Tsung, W. Huang and G. A. Somorjai, *J. Catal.*, 2009, **265**, 209–215.

43 S. Hu, C. Melton and D. Mukherjee, *Phys. Chem. Chem. Phys.*, 2014, **16**, 24034–24044.

44 S. Hu, M. Tian, E. L. Ribeiro, G. Duscher and D. Mukherjee, *J. Power Sources*, 2016, **306**, 413–423.

45 S. Hu, G. Goenaga, C. Melton, T. A. Zawodzinski and D. Mukherjee, *Appl. Catal., B*, 2016, **182**, 286–296.

46 M. Muniz-Miranda, C. Gellini, P. Canton, P. Marsili and E. Giorgetti, *J. Alloys Compd.*, 2014, **615**, S352–S356.

47 H. Zeng, X.-W. Du, S. C. Singh, S. A. Kulinich, S. Yang, J. He and W. Cai, *Adv. Funct. Mater.*, 2012, **22**, 1333–1353.

This journal is © The Royal Society of Chemistry 2017

Catal. Sci. Technol., 2017, **7**, 2074–2086 | **2085**

48 B. M. Hunter, J. D. Blakemore, M. Deimund, H. B. Gray, J. R. Winkler and A. M. Müller, *J. Am. Chem. Soc.*, 2014, **136**, 13118–13121.

49 V. Amendola and M. Meneghetti, *Phys. Chem. Chem. Phys.*, 2013, **15**, 3027–3046.

50 E. Giorgetti, P. Marsili, P. Canton, M. Muniz-Miranda, S. Caporali and F. Giammanco, *J. Nanopart. Res.*, 2013, **15**, 1360.

51 A. Matsumoto, A. Tamura, T. Honda, T. Hirota, K. Kobayashi, S. Katakura, N. Nishi, K.-I. Amano, K. Fukami and T. Sakka, *J. Phys. Chem. C*, 2015, **119**, 26506–26511.

52 S. Ibrahimkutty, P. Wagener, T. D. S. Rolo, D. Karpov, A. Menzel, T. Baumbach, S. Barcikowski and A. Plech, *Sci. Rep.*, 2015, **5**, 16313.

53 J. Lam, D. Amans, F. Chaput, M. Diouf, G. Ledoux, N. Mary, K. Masenelli-Varlot, V. Motto-Ros and C. Dujardin, *Phys. Chem. Chem. Phys.*, 2014, **16**, 963–973.

54 A. Matsumoto, A. Tamura, K. Fukami, Y. H. Ogata and T. Sakka, *J. Appl. Phys.*, 2013, **113**, 053302.

55 B. Kumar, D. Yadav and R. K. Thareja, *J. Appl. Phys.*, 2011, **110**, 074903.

56 D. Zhang, B. Gokce and S. Barcikowski, *Chem. Rev.*, 2017, **117**(5), 3990.

57 J. Lam, J. Lombard, C. Dujardin, G. Ledoux, S. Merabia and D. Amans, *Appl. Phys. Lett.*, 2016, **108**, 074104.

58 R. Tanabe, T. T. P. Nguyen, T. Sugiura and Y. Ito, *Appl. Surf. Sci.*, 2015, **351**, 327–331.

59 A. Tamura, A. Matsumoto, K. Fukami, N. Nishi and T. Sakka, *J. Appl. Phys.*, 2015, **117**, 173304.

60 V. Lazic, S. Jovicevic and M. Carpanese, *Appl. Phys. Lett.*, 2012, **101**, 054101.

61 S. Ibrahimkutty, P. Wagener, A. Menzel, A. Plech and S. Barcikowski, *Appl. Phys. Lett.*, 2012, **101**, 103104.

62 S. Scaramuzza, M. Zerbetto and V. Amendola, *J. Phys. Chem. C*, 2016, **120**, 9453–9463.

63 B. M. Hunter, J. D. Blakemore, M. Deimund, H. B. Gray, J. R. Winkler and A. M. Muller, *J. Am. Chem. Soc.*, 2014, **136**, 13118–13121.

64 V. Amendola, S. Scaramuzza, S. Agnoli, G. Granozzi, M. Meneghetti, G. Campo, V. Bonanni, F. Pineider, C. Sangregorio, P. Ghigna, S. Polizzi, P. Riello, S. Fiameni and L. Nodari, *Nano Res.*, 2015, **8**, 4007–4023.

65 S. Scaramuzza, S. Agnoli and V. Amendola, *Phys. Chem. Chem. Phys.*, 2015, **17**, 28076.

66 K. D. Malviya and K. Chattopadhyay, *J. Phys. Chem. C*, 2014, **118**, 13228–13237.

67 C. Rehbock, V. Merk, L. Gamrad, R. Streubel and S. Barcikowski, *Phys. Chem. Chem. Phys.*, 2013, **15**, 3057–3067.

68 M. E. Povarnitsyn, T. E. Itina, P. R. Levashov and K. V. Khishchenko, *Phys. Chem. Chem. Phys.*, 2013, **15**, 3108.

69 R. Intartaglia, G. Das, K. Bagga, A. Gopalakrishnan, A. Genovese, M. Povia, E. Di Fabrizio, R. Cingolani, A. Diaspro and F. Brandi, *Phys. Chem. Chem. Phys.*, 2013, **15**, 3075–3082.

70 E. Giorgetti, P. Marsili, P. Canton, M. Muniz-Miranda, S. Caporali and F. Giammanco, *J. Nanopart. Res.*, 2013, **15**, 1360.

71 E. Jiménez, K. Abderrafi, R. Abargues, J. L. Valdés and J. P. Martínez-Pastor, *Langmuir*, 2010, **26**, 7458–7463.

72 S. Hu, C. Melton and D. Mukherjee, *Phys. Chem. Chem. Phys.*, 2014, **16**, 24034–24044.

73 K. H. Solangi, S. N. Kazi, M. R. Luhur, A. Badarudin, A. Amiri, R. Sadri, M. N. M. Zubir, S. Gharehkhani and K. H. Teng, *Energy*, 2015, **89**, 1065–1086.

74 H. H. Liu, J. Lanphere, S. Walker and Y. Cohen, *Nanotechnology*, 2015, **26**, 045708.

2086 | *Catal. Sci. Technol.*, 2017, **7**, 2074–2086

This journal is © The Royal Society of Chemistry 2017